Applied Surface Science 679 (2025) 161180

Contents lists available at ScienceDirect

Applied Surface Science

journal homepage: www.elsevier.com/locate/apsusc

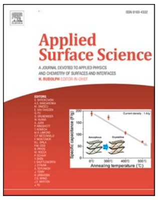

Modifying vacancy defects during systematic disordering of the Cr_2AlC nano-lamellar system

João S. Cabaço [a,f,*], Maciej Oskar Liedke [b], Javier Pablo-Navarro [c,d], Fabian Ganss [a], César Magén [c], Manuel Ricardo Ibarra [c,d], Ulrich Kentsch [a], Maik Butterling [b], Andreas Wagner [b], Jürgen Lindner [a], Jürgen Faßbender [a,e], Christoph Leyens [f], Richard Boucher [f], Rantej Bali [a]

[a] Institute of Ion Beam Physics and Materials Research, Helmholtz-Zentrum Dresden-Rossendorf, 01328 Dresden, Germany
[b] Institute of Radiation Physics, Helmholtz-Zentrum Dresden-Rossendorf, 01328 Dresden, Germany
[c] Instituto de Nanociencia y Materiales de Aragón (INMA), CSIC-Universidad de Zaragoza, 50018 Zaragoza, Spain
[d] Laboratory of Advanced Microscopies (LMA), University of Zaragoza, 50018 Zaragoza, Spain
[e] Institute of Solid State and Materials Physics, Technische Universität Dresden, 01069 Dresden, Germany
[f] Institute of Materials Science, Technische Universität Dresden, 01069 Dresden, Germany

ARTICLE INFO

Keywords:
Positron annihilation spectroscopy
Cr_2AlC
Vacancies
Lattice defects
MAX phases

ABSTRACT

The layered structure of MAX phases is associated with a number of functional properties and is the subject of extensive research. While the unit-cell layers of these structures have been well studied, much less is known about the distribution and manipulation of point defects within them. Here, we selected the prototype Cr_2AlC system and, using variable energy positron beams, observed Doppler broadening and positron annihilation lifetimes to track the evolution of defects caused by the penetration of energetic transition metal ions (Co^+ and Mn^+) and noble gas ions (Ar^+ and Ne^+). In all cases an overall reduction of the open-volume defect concentration is observed post-irradiation. Atomic displacements induced by the penetrating ions drastically modify the defect distribution: the concentration of agglomerates of 9–15 vacancies (corresponding to positron lifetimes of 335–450 ps) in the precursor $[Cr_2C/Al]n$ layers is suppressed, whereas Al mono- and Al-Cr di-vacancy (lifetimes 217–231 ps) concentrations are enhanced. This breakdown of large defects into point defects scales with atomic displacements and is largely independent of the penetrating ion species, providing insights into the manipulation of point defects in nano-layered systems.

1. Introduction

Materials design is often confronted with the problem of combining vastly different physical properties, such as in coatings requiring good thermal and electrical conductivity [1] as well as hardness [2,3]. One solution is to combine a ceramic unit-cell wide layer, often of a compound of a transition metal, 'M', with Carbon or Nitrogen, referred to as 'X'. In so called MAX phases the M_2X layers are separated by an atomic layer of A-group element such as Al, thus forming an M_2AX compound [4–6]. The crystallographic structure is hexagonal with space group $P6_3/mmc$, and can be viewed as possessing the …M_2X-A-M_2X-A… stacking sequence [7]. The promise of these materials is the combination of vastly differing properties. In recent years, MAX phases have been vigorously investigated for their applications, such as ceramic-like mechanical hardness [7–9], oxidation resistance [10], crack self-healing [11], and radiation resistance [7,12–14], as well as the metal-like electrical conductivity [15–17].

The unit-cell thickness of the M_2X layer and the single A-atomic planes implies that a point defect within the layers is sufficient to locally disturb the stacking sequence, potentially causing large changes to the properties. These disturbances can occur in various forms, one instance is through vacancies. In specific cases these defects can be useful, for example in absorbing irradiated particles in radiation protection applications [14,18]. However, these defects are unavoidable in MAX phase systems, in particular those which have found commercial applications, such as Cr_2AlC [19] and are prepared using industrially compatible methods such as magnetron sputtering. Since the presence of point defects may play a role in determining the functional properties of nano-layered systems, *i.e.* impacting the radiation tolerance properties [20], a microscopic characterization of defects is necessary.

---

* Corresponding author at: Institute of Ion Beam Physics and Materials Research, Helmholtz-Zentrum Dresden-Rossendorf, 01328 Dresden, Germany.
E-mail address: j.salgado-cabaco@hzdr.de (J.S. Cabaço).

https://doi.org/10.1016/j.apsusc.2024.161180
Received 17 June 2024; Received in revised form 20 August 2024; Accepted 5 September 2024

In the case of the M_2AX structure, knowledge of the type of vacancies and the response of the open volume defects to irradiation of particles such as ions is of fundamental interest. For instance, the implantation of 3*d* transition metals into the nano-layered system can act as scattering centers for electronic transport within the layers. Ion-irradiation is expected to modify the vacancy concentration as well, which can indirectly affect the transport behavior through vacancy diffusion and recombination thereby influencing the local environment of the implanted atom. Due to sensitivity issues, differentiating vacancy types, such as mono-, di- as well as larger vacancies is non-trivial, however can lead to insights such as the evolution of vacancies with increasing atomic displacements. The most suitable technique to probe such defects is positron annihilation spectroscopy with lifetime analysis [21]. The implanted positron lifetime is a function of the defect size, as well as its chemical surrounding, and can be simulated using *ab-initio* simulations [22].

In this work we focused on a prototype M_2AX system, Cr_2AlC in thin film form. The structural evolution due to disorder has been studied by several authors [7,12–14]. Starting from as-grown material, disordering was achieved through the use of ion irradiation with different elements and fluences. The rearrangement of the atoms due to disorder leads to the formation of C interstitials, as well as antisite defects (Cr_{Al} and Al_{Cr}) [13]. In fact, the ability of M and A atoms to exchange positions provides an efficient means for the accommodation of radiation-induced point defects [7]. In this system, disorder results in an expansion of the *c*-axis and to a contraction of the *a*-axis, leading to a distorted phase known as $\gamma - Cr_2AlC$. However, when it comes to information about open volume defects, such as vacancies, some questions remain unanswered. Although Q. Huang *et al.* [13] calculated the formation energies for different open-volume defects in this system, experiments probing those defects and how they evolve due to increased disorder are still unavailable in the literature.

In this paper, we probe vacancy defects formed in Cr_2AlC formed under systematic irradiation-induced disordering using 3d transition metal ions (Co^+ and Mn^+), which can bring about magnetic doping, and chemically inert Ne^+ and Ar^+ ions as controls, which lead only to disorder. Open volume defects in the irradiated Cr_2AlC films were investigated using Positron Annihilation Lifetime Spectroscopy (PALS) as well as Doppler Broadening Spectroscopy (DBS) of the positron annihilation absorption line. Through a comparison of the experimental results with ATSUP *ab-initio* simulations [22], various defect states, including mono- and di- vacancies, as well as agglomerates of vacancies were identified. Regardless of the irradiated ion species, agglomerates of 9–15 vacancies were transformed into Al mono-vacancies and Cr-Al di-vacancies, and, contrary to predictions [7,23], the overall concentration of open-volume defects decreased with ion-irradiation. Deviations from the above trend were observed in the case of Ne^+-ions, whereas the vacancy distributions under the Co^+, Mn^+ and Ar^+ irradiation showed similar behavior. For fundamental studies on the effects of 3*d* transition M_2AX system, the Ar^+ ion can therefore act as an effective control.

2. Materials and methods

Thin films of Cr_2AlC with $t = 50$ nm and $t = 500$ nm were prepared by magnetron sputtering onto a Si(1 1 1) substrate at room temperature. On top of Si a layer of 20 nm SiO_2 was grown (by thermal dry oxidation), followed by 80 nm of Si_3N_4 (by low pressure chemical vapor deposition). Si_3N_4 and SiO_2 act as diffusion barriers to suppress any interaction between the substrate and the multilayer system [24,25]. The deposition for the multilayer system was achieved using elemental targets, and a sequence of layers with 4 nm for Cr, 2 nm for Al and 2 nm for C, which was repeated 7 times to achieve $t = 50$ nm and 57 times to achieve $t = 500$ nm [24]. The Cr and Al layers were deposited at 200 W and 80 sccm Ar flow reaching a deposition rate of 2.03 nm/s and 1.56 nm/s, respectively. C layers were deposited at 450 W with the same Ar flow, reaching a deposition rate of 0.27 nm/s. Following deposition, the thin films were annealed at different temperature steps using a rapid thermal annealing (RTA) furnace. The annealing steps were made in an Ar atmosphere at 823 K, 923 K and 1173 K for a hold time of 30 s using a heating rate of 15 K/s.

The Monte Carlo simulation code SRIM [26] was used to fine-tune the irradiation energies and angle of incidence, with the standard displacement energies of 25 eV for Cr/Al and 28 eV for C [26]. To avoid surface effects or intermixing with the buffer layers, the quasi-Gaussian profile for the concentration of ions with depth was optimized to be in the central thickness of the thin-film, as seen in Fig. 1, right-axis. Energies of 250 keV to 400 keV were used for the $t = 500$ nm films and 25 keV to 50 keV for $t = 50$ nm. The displacements per atom, dpa profiles are shown in Fig. 1 left axis for both film thicknesses at a fluence of 1×10^{15} ions • cm^{-2}. The chosen ion species were transition metals (Co^+, Mn^+) and inert gas elements (Ar^+, Ne^+). Due to the different ion species used, and hence atomic mass, the peak dpa and dpa are different, and can be found in S1 of the supplementary material for the other fluences used, 1×10^{14} ions • cm^{-2} and 5×10^{15} ions • cm^{-2}.

Grazing incidence X-ray diffraction (GIXRD) was undertaken with a Rigaku SmartLab diffractometer with parallel beam optics and a Cu anode generating radiation with a wavelength of 0.154 nm. For microstructural characterization, high-resolution transmission electron microscopy (HRTEM), electron energy loss spectroscopy (EELS) and energy dispersive X-ray spectroscopy (EDX) were used. These analyses were performed in a probe-corrected FEI Titan Low Base operated at 300 keV, equipped with a high-brightness field emission gun (X-FEG) and a CETCOR aberration corrector for the probe from CEOS. In addition, the setup included an Ultim Max TLE10 EDX system by Oxford Instruments and a Gatan Imaging Filter Tridiem 866 ERS for EELS.

Doppler broadening spectroscopy (DBS) and positron annihilation lifetime spectroscopy (PALS) were used. For PALS, a monoenergetic positron beam is created by pair production at a tungsten target. The unique temporal resolution of the ELBE beam is transferred on the positron beam, resulting in a pulsed positron source with high repetition rate, high intensity and selectable implantation energy, allowing high depth resolution. The time resolution is 230 ps FWHM (or 102 ps RMS) timing resolution, and the total events collected in a spectrum are 10^7 counts. For Doppler broadening spectroscopy DBS, positrons are generated through β^+ decay of the radioisotope ^{22}Na, obtaining a monoenergetic beam after positron moderation that is accelerated towards the sample with selectable energy. The positron penetration depth (z), can be approximated, using the density (ρ) of the material and the implantation energy used (E_p), by the formula $z_{mean} = \left(\frac{36}{\rho}\right) \bullet E_p^{1.62}$ [27]. To achieve the required penetration depth, energies up to 12.5 keV could be

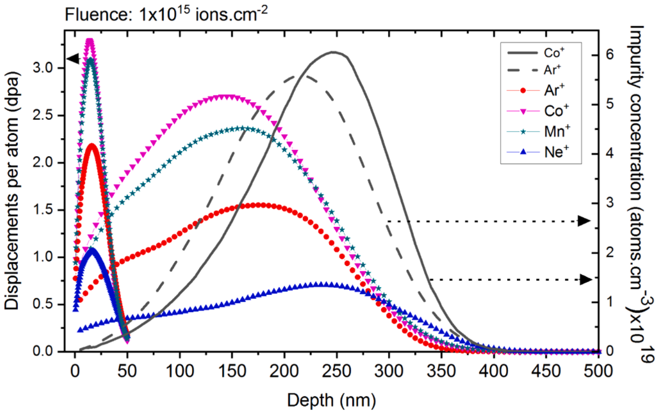

Fig. 1. Simulated dpa profile as a function of depth for t = 50 nm (peaks on the left) and t = 500 nm samples at a fixed fluence. The impurity concentration profile is represented in the right axis for Co^+ and Ar^+. Simulations were made using SRIM [26].

used. In addition, both DBS and PALS were done at room temperature.

When positrons are implanted, they dwell in open-volume defects, and then annihilate with electrons, thereby emitting at least 2γ photons [28,29]. The energy of the annihilation photon was measured using high purity Ge detectors, with a resolution better than 1.1 keV at 511 keV. For DBS the broadening of the annihilation profile was characterized using two different parameters: the S-parameter corresponds to the fraction of the annihilation line in the middle region, and the W-parameter is related to the fraction in the outer region. The S-parameter is suitable for the analysis of depth dependent defect concentrations and the W-parameter, being more sensitive to core electrons, the atomic environment of defects. Additionally, the PALS [30] technique allows for the decomposition of the lifetime distributions, revealing several lifetimes $\tau_1, \tau_2, \cdots \tau_i$, along with their associated intensities I(τ_2), I (τ_2), ..I (τ_i). By combining experimental results of positron lifetimes with atomic superposition (ATSUP) *ab-initio* simulations [22] for defect states, it was possible to identify different defects. Due to the complexity of the crystal only a non-optimized (no relaxations due to defects) structures were considered. DBS and PALS measurements were carried out at the AIDA setup [31] and the MePS beamline, respectively, at the ELBE (Electron Linac for beams with high Brilliance and low Emittance) facility at the Helmholtz-Zentrum Dresden-Rossendorf [32].

3. Results

3.1. Structural analysis

XRD on the as-grown and ion-irradiated thin films was done with a grazing incidence angle of 5° to increase the intensity diffracted by the films and suppress the contribution from the single crystal Si (1 1 1) substrate. In Fig. 2 a) and b) the diffractogram around the (0 0 2) reflection of Cr_2AlC are shown for the $t = 500$ nm and $t = 50$ nm samples, respectively. The main MAX-phase Cr_2AlC peaks are observed, namely, the (0 0 2), (1 0 2), (1 0 3) and (0 0 6). At ~ 43.6° secondary phase peaks are also seen, however, the presence of $AlCr_2$, Al_8Cr_5, Cr_7C_3 is often reported in MAX phase synthesis [33–36]. Following ion irradiation, the superstructure reflection (0 0 2) undergoes a decrease in intensity of approximately 50 % for the $t = 500$ nm sample. Contrastingly, for the $t = 50$ nm sample the superstructure reflection is completely suppressed after ion irradiation. Moreover, an additional peak appears around 40.2–40.7° in both film thicknesses. This new peak is associated with the (0 0 6) reflection of grains/crystallites featuring an expansion along the *c*-axis of up to 4 %. Similarly, a contraction along the *a*-axis would be expected [7,12,13], however, the low intensity of the (*h*00) and (hk0) reflections made it difficult to quantify, and the film strain might even compensate the contraction of grains whose *c*-axis is oriented in the film plane.

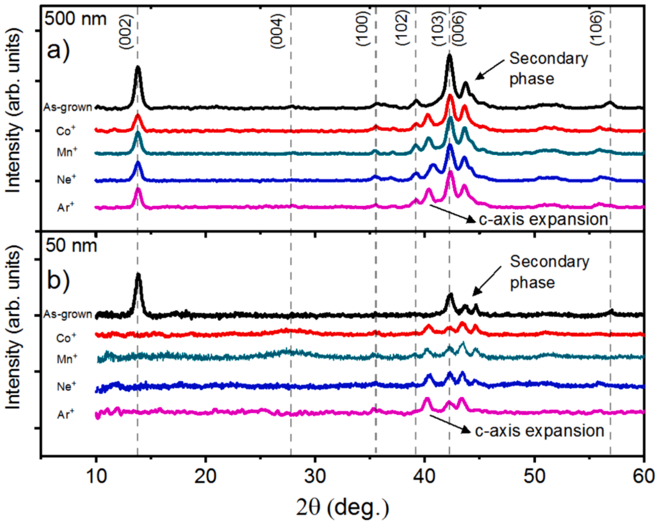

Fig. 2. Diffractograms of Cr_2AlC thin films for as-grown and irradiated samples at a fluence of 1×10^{15} ions • cm^{-2}. a) and b) show the results for the $t = 500$ nm and $t = 50$ nm samples, respectively.

Further microstructural analysis was made; in Fig. 3 a) and d) HRTEM cross sections of the as-grown $t = 500$ nm and $t = 50$ nm films are shown. The 500 nm film a) shows that growth occurs in a columnar fashion. For the 50 nm film it is difficult to confirm if the same behavior is present, due to the reduced thickness. Fast Fourier Transforms (FFT) of the HRTEM images collected along the (3, 3, −1) zone axis are shown for both as-grown $t = 500$ nm and $t = 50$ nm in c) and f), corresponding to an area of 15.1 × 15.1 nm^2 and 9.5 × 9.5 nm^2, respectively. In the two cases, characteristic MAX phase reflections can be indexed and are indicated. STEM-EELS chemical maps are represented in b) and e), and the distribution of Cr and C is proven to be homogeneous. After irradiation HRTEM shows no significant changes in the $t = 500$ nm film g), when compared with the as-grown film a). Additional analysis is provided in S2 of the supplementary material, showing values for the elemental compositions, obtained using EDX, with Cr, Al, C, as well as O present. For the as-grown samples a 1.78 ratio of Cr:Al was observed, whereas the ion irradiated samples show a ratio of 1.6 and 1.78 for Co^+ and Ar^+ irradiation, respectively. The difference in ratios is within the measurement accuracy.

3.2. Positron annihilation spectroscopy

Fig. 4 shows the S parameter as a function of the positron implanted energy (depth) for the as-grown and irradiated $t = 500$ nm samples. The uncertainties associated with the determination of S are represented by error bars on the y-axis; however, the errors are three orders of magnitude smaller than the value of S, making them barely visible. The central region $t = (60–240)$ nm is indicated on the plots, because it is not affected by surface effects or strain near the buffer layers. In the central region, the samples show a homogenous S value, with the as-grown sample having the highest average value (S=0.584). For the irradiated samples, in the lowest fluence used (1×10^{14} ions • cm^{-2}), there is a decrease in S for all the ion species, this effect is smaller for Mn^+ ion species. Increasing the fluence to (1×10^{15} ions • cm^{-2}) causes a further decrease in the S value across all ion species. Finally, at the highest fluence (5×10^{15} ions • cm^{-2}), S reaches its lowest value for all the ion species, with a similar effect for Ar^+, Mn^+ and Co^+ (S~0.567) but a less pronounced effect for Ne^+ (S=0.572). For the W-parameter, shown in the supplementary material S3, the behavior is essentially a mirror horizontal image of the S-parameter. In supplementary material S4 a short discussion of the S(W) plot is presented.

PALS data in Fig. 5 shows the weighted average positron lifetime for the $t = 500$ nm samples at an irradiation fluence of 1×10^{15} ions • cm^{-2} using inert ion species a) and 3d metal ions d). In b)/e) and c)/f) the uncertainties associated with the determination of lifetime and associated intensities, respectively, are represented by error bars in the y-axis direction. In this plot a weighted average of the individual lifetime components τ_1, τ_2, τ_3 and associated intensities I (τ_1), I(τ_2), I(τ_3) is shown, and calculated as $\tau_{av} = \frac{\sum_{i=1}^{3} \tau_i . I(\tau_i)}{\sum_{i=1}^{3} I(\tau_i)}$. The error for the weighted average τ_{av} is obtained by propagation of the errors associated with the measured lifetime and intensity contributions, although it appears large, it is around ~ 6 %. The lifetime analysis software shows that the model used adequately fits the data, with an average reduced $\chi^2 \sim 1.2$.

The results in Fig. 5 a) show a decrease in average positron lifetime when the as-grown sample 273 ps, is compared with the inert ion irradiated samples 258 ps. Conversely, the samples irradiated with 3d metal ions decrease only to 267 ps. The decrease in τ_{ave} is associated with an overall reduction of the open-volumes, as a consequence of irradiation, *i. e.* reduction of the average defect size.

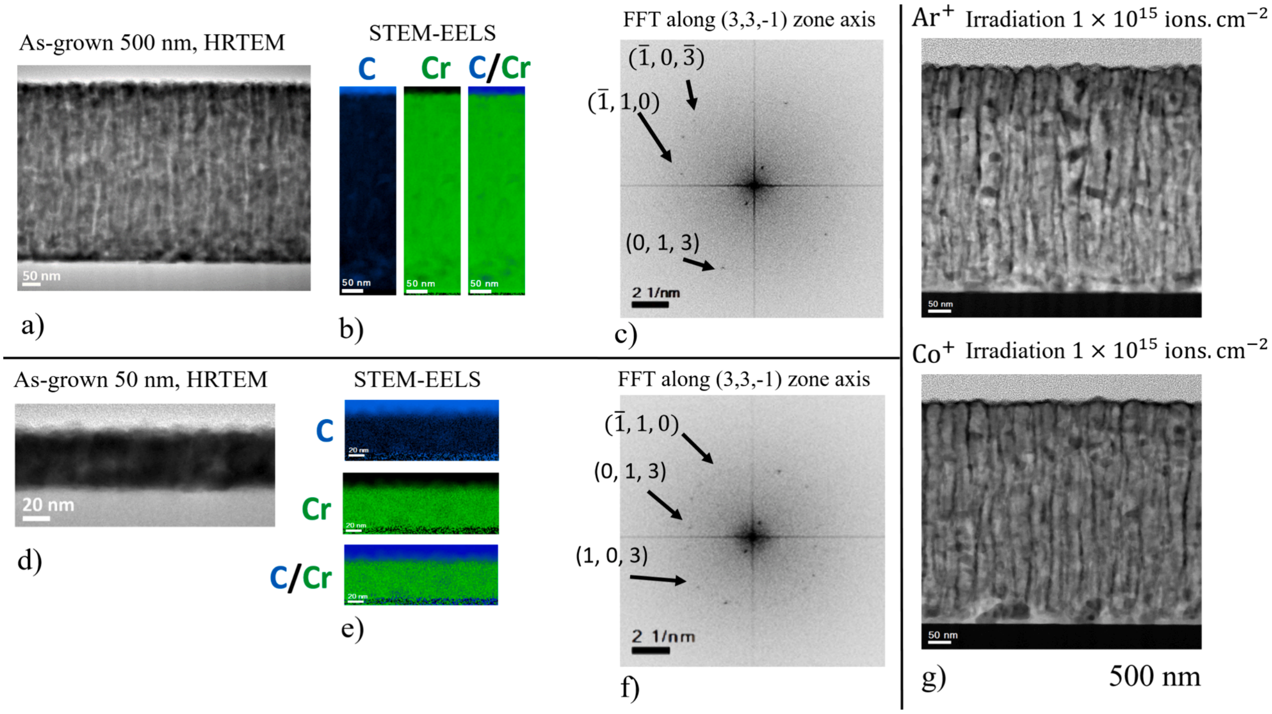

Fig. 3. Microstructural analysis of the Cr_2AlC films, showing HRTEM in a) and d) for as-grown $t = 500$ nm and $t = 50$ nm, along with the associated STEM-EELS chemical maps b) and e) and FFT along the (3,3,-1 zone axis) c) and f). In g) HRTEM is shown for $t = 500$ nm samples irradiated with Ar^+ and Co^+ at 1×10^{15} ions • cm^{-2}.

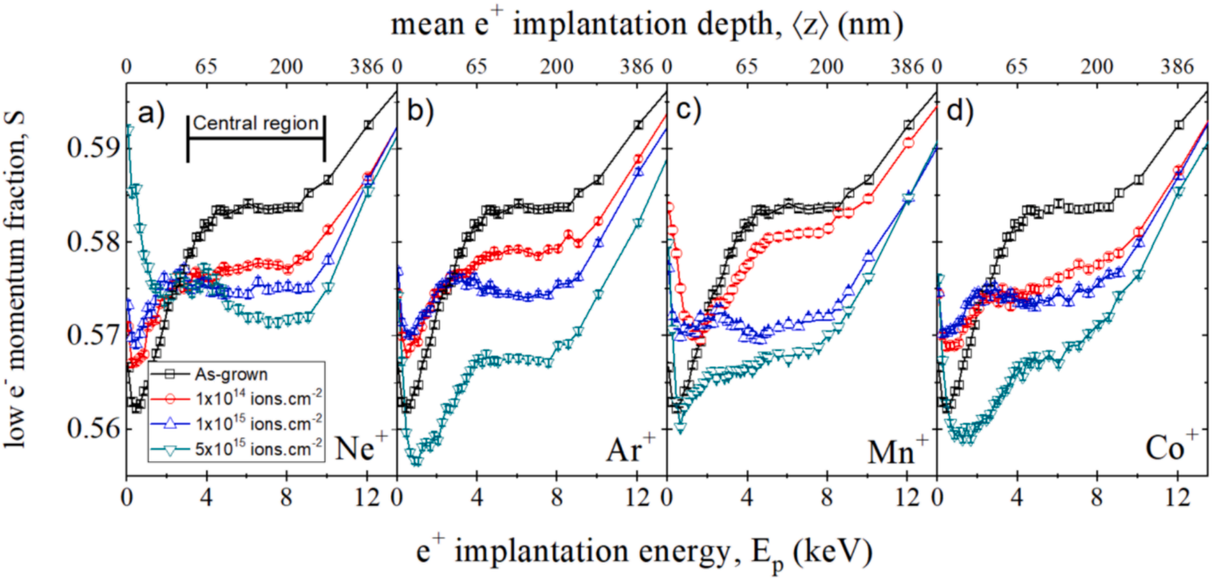

Fig. 4. DBS data for energy (depth) dependency of S- parameter in $t = 500$ nm samples irradiated at different fluences. The energy (depth) dependency of W-parameter is shown in supplementary material S3. The data for the as-grown films (open black squares) is the same in all panels for comparison.

Considering the individual lifetime components shown in Fig. 5 b) and e), there is an increase after irradiation across all ion species used, except for the case of Ne^+ irradiation. In Fig. 5 c) and f) the relative intensities associated with the individual lifetimes are shown. For τ_1, the intensity I (τ_1) is initially around 56 % for the as-grown sample, and increases to ~ 65 % for the Ne^+ irradiated sample and up to ~75 % for the Co^+, Mn^+ and Ar^+ ion species. Conversely, for the lifetime component τ_2, the relative intensity is around 40 % for the as-grown sample. Following irradiation there is a decrease to ~35 % for the Ne^+ ion species and down to 25–27 % for the Co^+, Mn^+ and Ar^+ ion species. The lifetime component τ_3 shows a relative intensity around 2 % in the as-grown sample, reducing to ~1 % for the Ne^+ ion species and nearly vanishes for the Co^+, Mn^+ and Ar^+ ion species (0–0.5 %). The decrease in weighted average positron lifetime represented in Fig. 5 a) and d) shows that the intensity is more determinant for the evaluation of the defect states than the lifetime. In other words, although the individual lifetimes increase after irradiation, as seen in b) and e), the increase in I (τ_1) and decrease in I(τ_2) and I(τ_3), as observed in c) and f), lower the overall τ_{ave}.

In Fig. 6 the relative intensities associated with the lifetimes τ_1, τ_2, τ_3

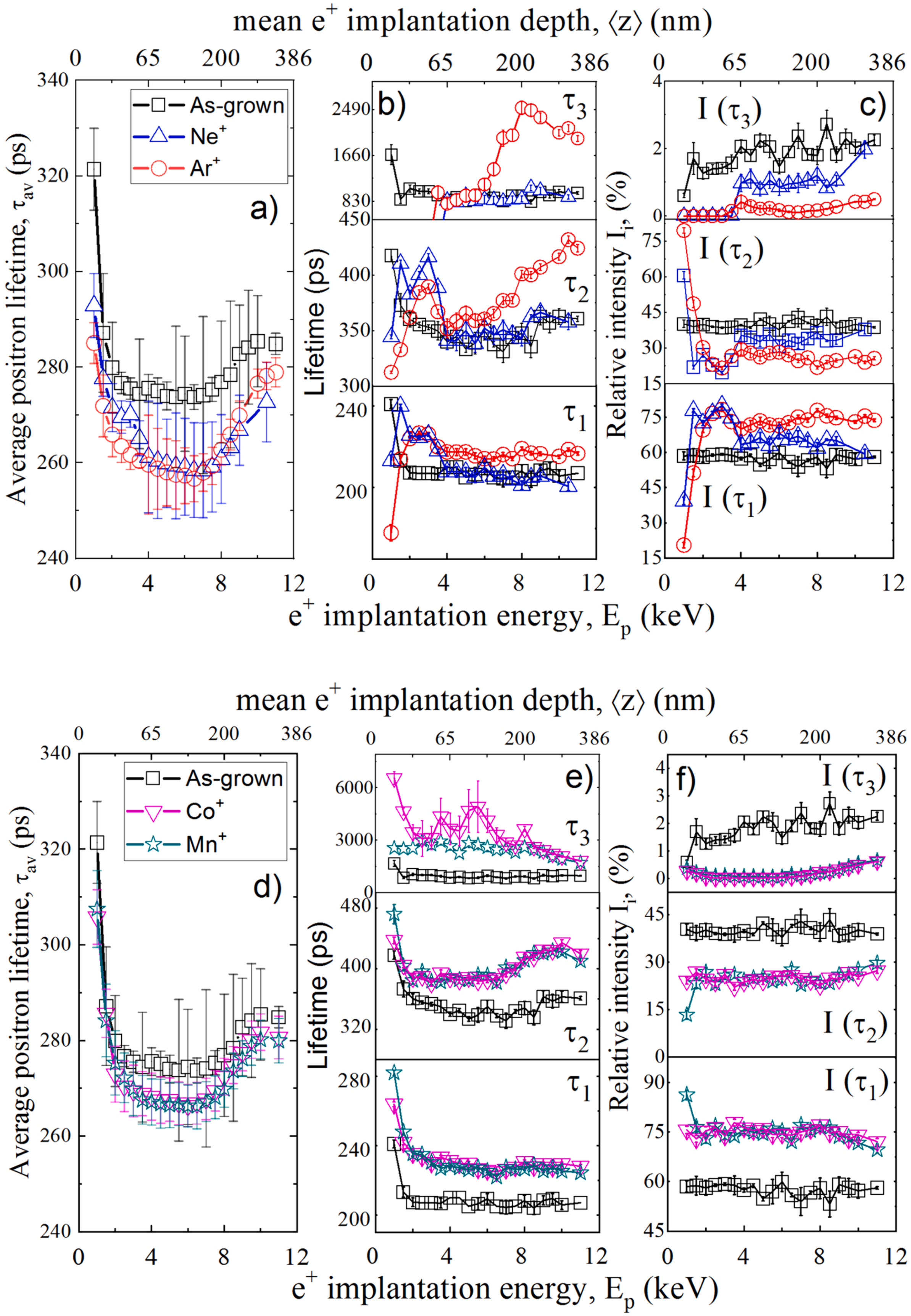

Fig. 5. PALS data for the as-grown $t = 500$ nm samples and ion irradiated samples at 1×10^{15} ions • cm^{-2} with inert ions a)-c) and transition metal ions d)-f). In a) and d) the weighted average positron lifetimes are shown, whereas b) and e) show the lifetimes of the three components $\tau_1 - \tau_3$ and associated intensities I(τ_1) – I(τ_3) in c) and f), respectively.

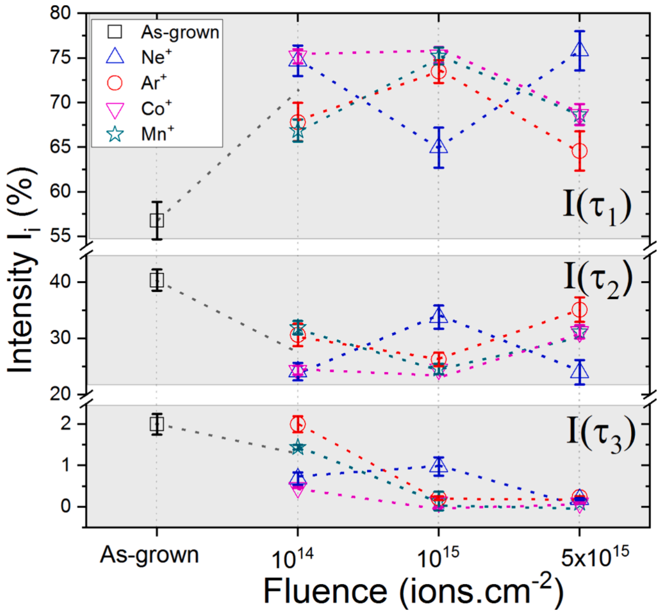

Fig. 6. PALS data representing intensity as a function of fluence for each of the individual lifetime components τ_1, τ_2 and τ_3 in the central region for $t = 500$ nm samples. As a guide to the eye, a dashed line connects the data associated with each ion species across the different fluences.

are shown for ion fluences 1×10^{14}, 1×10^{15} and 5×10^{15} ions • cm^{-2} in the central region $t = (60\text{–}240)$ nm. Across all ion species I (τ_1) increases after ion irradiation, saturating at 1×10^{15} ions • cm^{-2} for Ar$^+$, Co$^+$ and Mn$^+$ (~75 %), and at 5×10^{15} ions • cm^{-2} for Ne$^+$ (~76 %). For the second lifetime component, τ_2, the associated intensity decreases across all ion species, reaching its lowest value at 1×10^{15} ions • cm^{-2} for Ar$^+$, Co$^+$ and Mn$^+$ (~25 %), and at 5×10^{15} ions • cm^{-2} for Ne$^+$ (~22 %). For τ_3, the associated intensity, I(τ_3), reaches its lowest value for the fluence 5×10^{15} ions • cm^{-2} in all the ion species.

The τ_3 corresponds to long lifetimes in the 450–5000 ps range, suggesting the presence of large voids, porosity or amorphous regions. From the TEM data in Fig. 3 it can be inferred that these voids occur in the regions between the columnar grains. The granular structure is further confirmed from the broadening of the XRD reflections. Furthermore, the low, ~2 % intensity of the τ_3 signal is consistent with the predominantly crystalline structure of the films and also makes the identification of the effect that causes it to be difficult.

A similar analysis was extended to the $t = 50$ nm samples, focusing on a fluence of 1×10^{15} ions • cm^{-2}. In Fig. 7 a)-b) the DBS data is represented. The energy dependence of the S-parameter in the central region shows a behavior that differs from the central region of the $t = 500$ nm samples seen in Fig. 4. That is, the as-grown sample exhibits the lowest S-parameter value, whereas the ion-irradiated samples show an increase in S of ~0.06–0.1. However, a comparison of similar depths in the $t = 500$ nm samples shows that at $t = (0\text{–}41)$ nm the behavior is essentially the same as in the $t = 50$ nm films.

An analysis of the intensities associated with the individual lifetimes τ_1, τ_2 and τ_3, obtained with PALS, is shown in Fig. 7 c) for $t = 50$ nm in the central region. For the as-grown sample, I(τ_1) is initially ~50 %, and after ion irradiation increases to 59 % for the Mn$^+$ ion species, 63 % for the Co$^+$ and Ne$^+$ and 68 % for Ar$^+$. For the lifetime component τ_2, the associated intensity decreases from ~47 % in the as-grown sample to 40 % for the Mn$^+$ ion species, 37 % for the Co$^+$ and Ne$^+$ and 31 % for the Ar$^+$ species. I(τ_3) decreases from 2.5 % in the as-grown sample to 0.5–1 % for all the ion species. In summary, the PALS and DBS analyses for the $t = 500$ nm and $t = 50$ nm samples show a similar trend.

4. Discussion

Theoretical calculations for the positron lifetimes in different defect states were made by employing the ATomic SUPerposition (ATSUP) code [22]. The calculation enables the use of two different schemes, the Boronski-Nieminen (BN) parametrization and the Gradient Correction (GC); more details can be found in [30,34]. For the defect-free material the lattice parameters $a = b = 2.85$ Å, $c = 12.82$ Å and density $\rho = 5.22$ g • cm^{-2} were used [37]. The point defects were modeled using a 128 atom based supercell. To ensure efficient convergence of the results concerning the positron parameters for point defects, the calculations employed a Brillouin-zone integration over the lowest-lying positron state, as explained in [37]. This approach effectively accounts for the supercell size, leading to rapid convergence of the outcomes.

As an initial assumption for which open-volume defects would more likely be present in Cr_2AlC, the predictions made by Q. Huang *et al.* [13] were taken into account, namely, the fact that C, Al and Cr vacancies have the lowest theoretically estimated formation energy. Considering

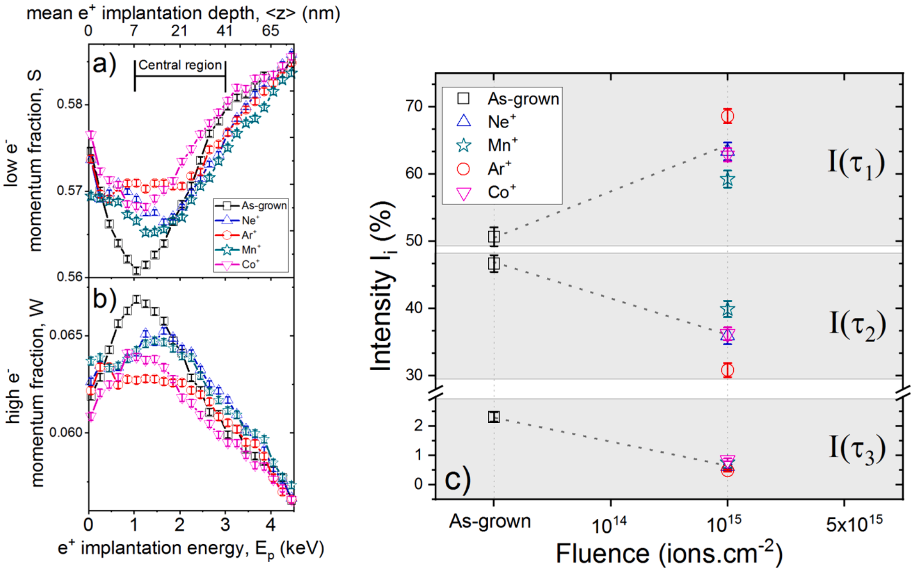

Fig. 7. DBS data for the $t = 50$ nm samples at 1×10^{15} ions • cm^{-2}, a)-b) shows the energy dependency of the S- and W- parameters. c) Represents the intensity of the individual lifetime components, obtained from PALS as a function of fluence for the central region.

that increasing levels of disorder are expected, mono-, di- and triple-vacancies, as well as agglomerates of up to 15 vacancies were considered in the simulations. The calculations for the different defect states considered are available in S6 of the supplementary material. The defect-free material was estimated to have a lifetime of 136 ps, whereas for mono-vacancies of Cr and Al the estimated lifetimes are 187 ps and 219 ps, respectively. It should be noted that the mono-vacancy of C cannot be identified experimentally due to its positive charge. Di-vacancies of Cr-C and Al-Cr were simulated and their lifetimes are 198 ps and 230 ps, respectively. Agglomerates of 9–15 vacancies were also simulated and found to have lifetimes ranging from 330 to 450 ps.

In the supplementary material S5 and S6 the experimental and simulated lifetime values can be found. Combining these lifetimes, dpa and change of intensities with respect to the as-grown component ($\Delta I = I(\tau_i) - I(\tau_i)_{as-grown}$), the 3D histogram shown in Fig. 8 a) was created. The lines on the lifetime axis show the average lifetime values for Al vacancies, Cr-Al di-vacancies, and agglomerates of 9–15 vacancies obtained by averaging the BN and GC scheme values. In b) the change in intensity is plotted as a function of lifetime. The simulations for defect-free Cr_2AlC predict a positron lifetime of 134–138 ps; however, no samples exhibit lifetimes in this range. The experimentally obtained τ_1 values for the as-grown samples fall in the range of 202–222 ps. Therefore, it can be concluded that the as-grown samples are not defect-free. In this experimental lifetime range, the Cr − C di-vacancies and Al vacancies are the closest match. However, Al vacancies have a higher binding energy, increasing the probability of being present. The ion irradiated samples show a maximum increase of τ_1 for a fluence of 1×10^{15} ions • cm^{-2} in all ion species. At such a fluence, they exhibit experimental lifetimes τ_1 between 205 ps and 235 ps. Although the ranges are those of simulated Cr − C di-vacancies, Al − Cr di-vacancies and Al-vacancies, the overlap of experimental and simulated data is highest for Al-Cr and Al vacancies, as well as the binding energies. The lifetime component τ_2 appears in the 320–430 ps range for both as-grown and irradiated samples. This range corresponds to simulated defect states consisting of large agglomerates with 9–15 vacancies. However, due to the calculation scheme used (BN or GC), each of these defect states has an estimated lifetime range of 30 to 40 ps. As a result, it is difficult to quantify which vacancy agglomerate is more likely, given the overlapping lifetimes and similar binding energies. In Fig. 8 c) the change in intensity as a function of dpa is represented for all the samples. As can be seen in the 3D histogram, the positive components, with a lifetime τ_1, associated with small defects, increase following irradiation, whereas the second lifetime τ_2, associated with agglomerates of 9–15 vacancies, decreases. For the lifetime component τ_3, the overall intensities are on the order of ~2 %, so they were omitted in this analysis.

After ion irradiation, the superstructure reflection (002) remains present only in the $t = 500$ nm film; however, the (006)/(103) reflections are observed for both film thicknesses. A part of the (006) reflection, shown in Fig. 2 a) and b), shifts to lower 2θ angles, which corresponds to an expansion of the *c*-lattice parameter of up to 4 %. This expansion means there is a distortion of the unit cell, and indicates a transformation to the $\gamma - Cr_2AlC$ phase. It has been shown [12] that the rearrangement of atoms due to irradiation leads to the appearance of a distorted phase with a different interlayer spacing, consequently, new reflections appear at 40.90°, 56.25° and 67.15° (2θ), identified as corresponding to (002), (102) and (110) planes, respectively. In this study, however, only the (002) reflection can be identified for the new phase.

The intensity of the (002) superstructure reflection of Cr_2AlC decreases by approximately 50 % after ion irradiation in the $t = 500$ nm films, and it completely disappears in the $t = 50$ nm films. A possible explanation for this effect can be obtained from the SRIM simulations shown in Fig. 1. Although the peak dpa at the same fluence is only slightly higher for the $t = 50$ nm film than for the $t = 500$ nm, the distribution of dpa across the film thickness is significantly different. For $t = 50$ nm the dpa remains consistently high, contrastingly, for the $t = 500$ nm it falls below 0.5 for $t > 275$ nm. Moreover, for the same fluence (1×10^{15} ions • cm^{-2}), the average dpa per thickness is 1.23 dpa/nm for $t = 50$ nm, whereas it is only 0.71 dpa/nm for the $t = 500$ nm samples. This effectively means that the layered structure is completely disordered in the $t = 50$ nm film, whereas in the $t = 500$ nm film it is disordered in the 0–250 nm region but remains almost unaffected at higher depths. Consequently, the intensity of the superstructure reflection is completely suppressed in the former and only attenuated in the

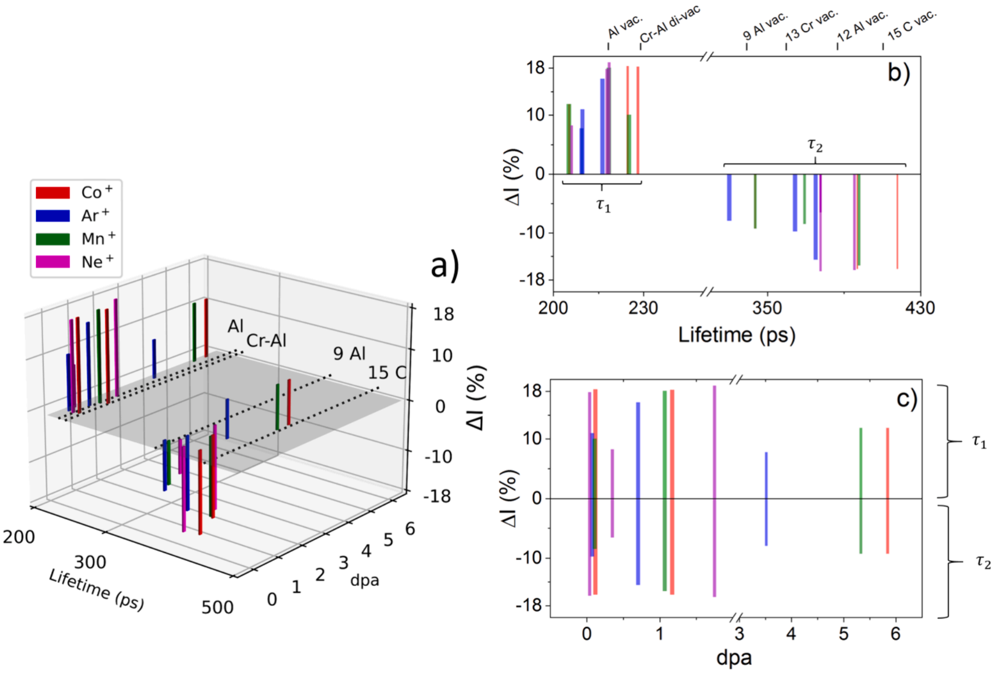

Fig. 8. a) 3d histogram showing the lifetime, dpa and change in intensity (ΔI) for the ion-irradiated samples, using as reference the values for the as-grown samples. b) and c) show the plots for ΔI as a function of lifetime and dpa, respectively. On top x-axis of b) the simulated positron lifetimes are represented for different defect states.

latter.

Contrary to some studies where similar peak dpa values led to amorphization [7,38], in our work this did not occur. For the $t = 500$ nm films irradiated with Co^+ at 5×10^{15} ions • cm^{-2} a 13.5 peak dpa was achieved. In contrast, for the $t = 50$ nm film at 1×10^{15} ions • cm^{-2}, the maximum was 3.3 peak dpa. A possible explanation for the high radiation tolerance can be the preexistence of amorphous regions and secondary phases [14]. It was suggested that amorphous nano-phases mitigate the accumulation of displacement damage effects, preventing amorphization and thus acting as a "self-healing capability" under high radiation environments. In this work, as we saw from the microstructural analysis and PALS data, some amorphous regions are present, which seem to enhance radiation tolerance and explain the high dpa achieved without amorphization. Further microstructural analysis with TEM and STEM/EELS, seen in Fig. 3, do not show any significant structural changes after ion irradiation. Moreover, the distribution of the elements is proven homogenous throughout the film depth and the ratios of Cr:Al are unaffected by ion irradiation, within the experimental error.

The DBS profile in Fig. 4 for the $t = 500$ nm samples shows a systematic decrease in the S-parameter for all ion species as fluence increases. For small thicknesses in the $t = 500$ nm samples (close to the film/substrate interface) the behavior is similar to what is seen for the $t = 50$ nm samples in Fig. 7 a). The S-parameter scales with the concentration of defects [39], therefore the defect concentration is in fact decreasing after irradiation in the central region. Due to a reduction in defect concentration, or, more specifically, a reduction in open-volumes, the positron diffusion length concomitantly increases, which, in turn, increases the annihilation fraction of positrons with the surface states and Si_3N_4/SiO_2 buffer layers. For the thinner film ($t = 50$ nm), the superposition of positron annihilation inside the film, at the surface, and at the Si_3N_4/SiO_2 buffer layer is unavoidable and contributes to the S-value. Therefore, the increase in S for the $t = 50$ nm film, seen in Fig. 7 a), can be attributed to a greater positron annihilation within the amorphous buffer, which itself has a larger S-value than the film [40,41].

The depth profiles simulated using SRIM in Fig. 1 show a pseudo-Gaussian distribution for both vacancy and ion concentration profiles, peaking around 130–260 nm for the $t = 500$ nm samples. However, DBS experiments, see Fig. 4, revealed a uniform defect concentration in the central region. This comparison suggests that the actual physical behavior is more complex than predicted by SRIM, with defects redistributing throughout the sample volume after irradiation.

Fig. 5 shows the results obtained from PALS for the $t = 500$ nm samples. A decrease in the weighted average positron lifetime is seen across all ion species used at a fluence of 1×10^{15} ions.cm^{-2}. The decrease in τ_{av} is associated with a reduction in open-volume defect size, induced by the irradiation process, and is more pronounced for the samples irradiated with inert ions than for the 3d ion irradiated samples. A possible explanation for this behavior can be that for 3d ions there is in fact substitution of some atomic lattice positions by the implanted ion, and the defects created in the surrounding are less effective at trapping positrons, hence the increased τ_{av} compared with inert ion irradiation. Another argument supporting this hypothesis is based on M(H) measurements of samples treated with both types of ions [42]. The increase in magnetization for samples irradiated with 3d ions is higher than for those irradiated with inert ions at the same dpa, suggesting that there is some incorporation of 3d ions in the lattice.

Additionally, the deconvolution of the PALS lifetime components shows an increase in the intensity associated with small defects I(τ_1) and a concurrent decrease in the intensity of large defects I(τ_2), I(τ_3) post-irradiation. The results in Fig. 6 show that for all ion species used for irradiation, except Ne^+, there is a saturation of the effects at a fluence of 1×10^{15} ions.cm^{-2}. In the case of Ne^+ the saturation occurs at a higher fluence, which is due to the lower values of dpa reached during irradiation. A closer examination of the dpa values in supplementary material S1 reveals that for a fluence of 1×10^{15} ions.cm^{-2}, the dpa is 0.35 for Ne^+, whereas for the other ion species, the dpa exceeds 0.7 at the same fluence. This difference can be attributed to the lower atomic weight of Ne^+.

The intensity of I(τ_1) reaches a maximum (75 %), and I (τ_2) and I(τ_3) reach a minimum of 25 % and ~0 %, respectively. The τ_3 component is associated with the amorphous fraction, likely located at the inter-columnar regions. A reduction in τ_3 suggests a re-arrangement of the voids in these regions, which could serve as traps for interstitials.

The experimental lifetimes obtained for the separated components of PALS data were compared with *ab-initio* ATSUP [22] simulations. It is shown in Supplementary Material S5 and S6 that the as-grown films of $t = 50$ nm and $t = 500$ nm are far from the ideal defect free case, with the presence of large vacancy agglomerates as well as mono and di-vacancies. By considering the simulations, the most likely small defect present in the as-grown samples are Al mono-vacancies. For large defect agglomerates, the overlap of experimental lifetimes with different simulated clusters makes it difficult to quantify which are present in the samples. Ion irradiation causes the large agglomerates of 9–15 vacancies to transform into mono-vacancies of Al and di-vacancies of Cr-Al. This transformation is maximized at a fluence of 10^{15} ions • cm^{-2} for all samples except the one irradiated with Ne^+ (at lower dpa). Above this fluence the intensity associated with small defects starts decreasing and, simultaneously, the intensity associated with large defects increases. This shows that during the dynamic evolution of open-volume defects in Cr_2AlC it is possible to transform large agglomerates of vacancies into smaller defects using selected ion fluences. For the $t = 50$ nm samples, the similarity between Fig. 6 and Fig. 7 c) suggests the same behavior occurs for both film thicknesses.

Insights into the local environment of the vacancies, as characterized by the ratio of high and low momentum electrons were obtained using S-W plots (Fig. S3 in Supplementary Material). For each investigated ion-species, the S-W points tend to fall on a straight line with negative slope. The linear behavior is an indication that the local vacancy environment does not vary with increasing ion-fluence. However, any change in slope is an indication of a shift in the local environment. Extrapolation of the slopes relative to the slope for the S-W of the as-grown films indicates whether the local environment under irradiation diverges from that of the as-grown state. As seen in Figure S3, the S-W line corresponding to Mn^+ and Ne^+ irradiation can be extrapolated to the S-W of the as-grown sample, suggesting a preserved local environment. The Co^+ and Ar^+ lines diverge from the as-grown reference, showing that these ions modify the local vacancy environment. Moreover, the S-W lines for Co^+ and Ar^+ nearly overlap, further suggesting that Ar^+ is indeed a valid control irradiation species for studying any property variations due to the Co^+. Further analysis of the high electron momentum fraction, to some extent indicated by the W-parameter, will require techniques such as coincidence Doppler broadening and are anticipated as part of future investigations.

According to the literature [7], early-stage irradiation in MAX phase materials typically results in the presence of isolated point defects, such as interstitials or vacancies. As the fluence of irradiation increases, these defects tend to cluster and form extended defects. Although the number of point defects is observed to increase with irradiation in our work, we find that this is due to a transformation of large defect clusters into mono- and di-vacancies, which is shown in the simplified schematic of Fig. 9. Moreover, it is observed that the defect size and concentration of open-volume defects decreases post-irradiation, which has not been seen in the literature. The ability to use ion irradiation at selected fluences to decrease the size of defects can be useful in enhancing the material's mechanical and thermal properties, thereby increasing its resilience in structural damage due to prolonged use [14]. Ultimately, the increased stability and durability expand its applications in demanding environments, such as encountered in aerospace or nuclear industries [43–50].

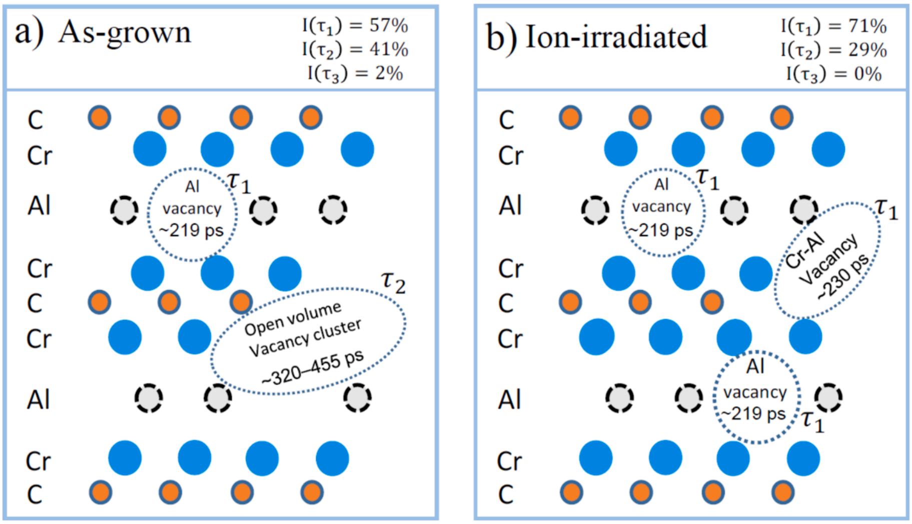

Fig. 9. Schematic illustration for the defect state evolution of open-volume defects in Cr_2AlC, before a) and after ion irradiation (1×10^{15} ions • cm^{-2}) b). The intensities associated with each type of defect are indicated, as well as the lifetimes.

5. Conclusion

In order to modify open-volume defects in nano-lamellar Cr_2AlC, systematic disorder using transition metal ions and noble gas as control was induced. Despite the suppression of the nano-lamellar structure a reduction in overall open-volume defect size and concentration is observed. The distribution of defects was observed through a combination of positron-annihilation spectroscopy and *ab-initio* simulations. With increasing atomic displacements large agglomerates of 9–15 vacancies, with positron lifetimes of 335–450 ps, present in the as-grown Cr_2AlC, transform into Al mono- and Al-Cr di-vacancies with positron lifetimes of 217–231 ps. Our results show that using ion irradiation at selected fluences could potentially be used to reduce the large defect agglomerates to point defects.

CRediT authorship contribution statement

João S. Cabaço: Writing – original draft, Investigation, Data curation, Conceptualization. **Maciej Oskar Liedke:** Writing – review & editing, Software, Investigation, Data curation, Conceptualization. **Javier Pablo-Navarro:** Writing – review & editing, Software, Investigation. **Fabian Ganss:** Writing – review & editing, Software, Investigation. **César Magén:** Writing – review & editing, Investigation. **Manuel Ricardo Ibarra:** Writing – review & editing, Investigation. **Ulrich Kentsch:** Writing – review & editing, Investigation. **Maik Butterling:** Writing – review & editing, Software, Investigation. **Andreas Wagner:** Writing – review & editing, Supervision, Funding acquisition. **Jürgen Lindner:** Writing – review & editing, Supervision, Funding acquisition. **Jürgen Faßbender:** Writing – review & editing, Supervision, Funding acquisition. **Christoph Leyens:** Writing – review & editing, Supervision, Funding acquisition. **Richard Boucher:** Writing – review & editing, Supervision, Funding acquisition, Conceptualization. **Rantej Bali:** Writing – review & editing, Supervision, Funding acquisition, Conceptualization.

Declaration of competing interest

The authors declare that they have no known competing financial interests or personal relationships that could have appeared to influence the work reported in this paper.

Data availability

Data will be made available on request.

Acknowledgement

This work is supported by the German Science Foundation (DFG) through TRANSMAX project number 456078299. J.P.-N., C.M. and M.R. I. gratefully thank the European Union's Horizon 2020 research and innovation programme for the grant agreement no. 823717-ESTEEM3, and the regional Gobierno de Aragón for projects E13_23R and E28_23R. The authors acknowledge the use of instrumentation provided by the National Facility ELECMI ICTS, node Laboratorio de Microscopias Avanzadas (LMA) at Universidad de Zaragoza. The authors would also like to acknowledge the team of the Ion Beam Center at the Helmholtz–Zentrum Dresden – Rossendorf for performing the ion irradiation. Parts of this research were carried out at ELBE at the Helmholtz – Zentrum Dresden – Rossendorf e.V., a member of the Helmholtz Association. We would like to thank the facility staff for assistance. This work was partially supported by the Initiative and Networking Fund of the Helmholtz Association (FKZ VH-VI-442 Memriox), and the Helmholtz Energy Materials Characterization Platform (03ET7015).

Appendix A. Supplementary material

Supplementary data to this article can be found online at https://doi.org/10.1016/j.apsusc.2024.161180.

References

[1] W. Cui, F. Du, J. Zhao, W. Zhang, Y. Yang, X. Xie, Y.-W. Mai, Improving thermal conductivity while retaining high electrical resistivity of epoxy composites by incorporating silica-coated multi-walled carbon nanotubes, Carbon 49 (2011) 495–500, https://doi.org/10.1016/j.carbon.2010.09.047.

[2] G. Sundararajan, D. Sen, G. Sivakumar, The tribological behavior of detonation sprayed coatings: the importance of coating process parameters, Wear 258 (2005) 377–391, https://doi.org/10.1016/j.wear.2004.03.022.

[3] D.S. Rickerby, S.J. Bull, Engineering with surface coatings: The role of coating microstructure, Surf. Coat. Technol. 39–40 (1989) 315–328, https://doi.org/10.1016/0257-8972(89)90065-0.

[4] M.W. Barsoum, The M_{N+1} AX_N phases: a new class of solids: thermodynamically stable nanolaminates, Prog. Solid State Chem. 28 (2000) 201–281, https://doi.org/10.1016/S0079-6786(00)00006-6.

[5] W. Jeitschenko, H. Nowotny, F. Benesovsky, Kohlenstoffhaltige ternäre Verbindungen (H-Phase), Monatsh. Chem. 94 (1963) 672–676, https://doi.org/10.1007/BF00913068.

[6] W. Jeitschenko, H. Nowotny, F. Benesovsky, Die H-Phasen Ti_2TlC, Ti_2PbC, Nb_2InC, Nb_2SnC und Ta_2GaC, Monatsh. Chem. 95 (1964) 431, https://doi.org/10.1007/BF00901306.

[7] C. Wang, C.L. Tracy, R.C. Ewing, Radiation effects in $M_{n+1}AX_n$ phases, Appl. Phys. Rev. 7 (2020) 041311, https://doi.org/10.1063/5.0019284.

[8] B. Manoun, S.K. Saxena, M.W. Barsoum, High pressure study of Ti_4AlN_3 to 55 GPa, App. Phys. Lett. 86 (2005) 101906, https://doi.org/10.1063/1.1875750.

[9] B. Manoun, S.K. Saxena, T. El-Raghy, M.W. Barsoum, High-pressure X-ray diffraction study of Ta_4AlC_3, Appl. Phy. Lett. 88 (2006) 201902, https://doi.org/10.1063/1.2202387.

[10] Z. Feng, P. Ke, Q. Huang, A. Wang, The scaling behavior and mechanism of Ti_2AlC MAX phase coatings in air and pure water vapor, Surf. Coat. Technol. 272 (2015) 380–386, https://doi.org/10.1016/j.surfcoat.2015.03.037.

[11] A.-S. Farle, C. Kwakernaak, S. van der Zwaag, W.G. Sloof, A conceptual study into the potential of $M_{n+1}AX_n$-phase ceramics for self-healing of crack damage, J. Eur. Ceram. Soc. 35 (2015) 37–45, https://doi.org/10.1016/j.jeurceramsoc.2014.08.046.

[12] C. Wang, T. Yang, J. Xiao, S. Liu, J. Xue, Q. Huang, J. Zhang, J. Wang, Y. Wang, Structural transitions induced by ion irradiation in V_2AlC and Cr_2AlC, J. Am. Ceram. Soc. 99 (2016) 1769–1777, https://doi.org/10.1111/jace.14118.

[13] Q. Huang, H. Han, R. Liu, G. Lei, L. Yan, J. Zhou, Q. Huang, Saturation of ion irradiation effects in MAX phase Cr_2AlC, Acta Mater. 110 (2016) 1–7, https://doi.org/10.1016/j.actamat.2016.03.021.

[14] M.A. Tunes, M. Imtyazuddin, C. Kainz, S. Pogatscher, V.M. Vishnyakov, Deviation from the pure MAX phase concept: radiation-tolerant nanostructured dual-phase Cr_2AlC, Sci. Adv. 7 (2021), https://doi.org/10.1126/sciadv.abf6771.

[15] J. E. Yoo, J. Y. Sung, J. H. Hwang, I. Maeng, S.-J. Oh, I. Lee, Ji. H. Shim, S. Dug. Kim, Du.-S. Yoon, S. Y. Jang, Y. J. Kang, S. W. Lee, MAX-Phase films overcome scaling limitations to the resistivity of metal thin films, ACS Appl Mater Interfaces 13 (2021), 61809-61817. doi: 10.1021/acsami.1c20516.

[16] T. Ouisse, D. Pinek, M.W. Barsoum, Modelling in-plane magneto-transport in Cr_2AlC, Ceram. Int. 45 (2019) 22956–22960, https://doi.org/10.1016/j.ceramint.2019.07.339.

[17] J.D. Hettinger, S.E. Lofland, P. Finkel, T. Meehan, J. Palma, K. Harrell, S. Gupta, A. Ganguly, T. El-Raghy, M.W. Barsoum, Electrical transport, thermal transport, and elastic properties of M_2AlC (M=Ti, Cr, Nb and V), Phy. Rev. B 72 (2005) 115120, https://doi.org/10.1103/PhysRevB.72.115120.

[18] H. Han, D. Wickramaratne, Q. Huang, J. Dai, T. Li, H. Wang, W. Zhang, P. Huai, A first-principles study on the defective properties of MAX-phase Cr_2AlC: the magnetic ordering and strong correlation effect, RSC Adv. 6 (2016) 84262–84268, https://doi.org/10.1039/C6RA15366F.

[19] P. Liu, M. Hu, L. Hu, M. Yin, H. Wu, M. Hu, Fabrication of Cr_2AlC powder by molten salt electrolysis at 850 °C with good oxidation resistance, J. Alloy. Compd. 826 (2020) 154003, https://doi.org/10.1016/j.jallcom.2020.154003.

[20] W. Ling, K. Lai, J. Chen, F. Guo, D. Kang, Z. Zhao, J. Dai, Point defects and hydrogen-permeation behavior of MAX phase Cr_2AlC coating by first-principles studies, Nucl. Mater. Energy 36 (2023) 191486, https://doi.org/10.1016/j.nme.2023.101486.

[21] K. Saarinen, P. Hautojarvi, C. Corbel, Positron annihilation spectroscopy of defects in semiconductors, Semiconduct. Semimet. 51 (1998) 209–285, https://doi.org/10.1016/S0080-8784(08)63057-4.

[22] M.J. Puska, R.M. Nieminen, Defect spectroscopy with positrons: a general calculational method, J. Phys. F 13 (1983) 333, https://doi.org/10.1088/0305-4608/13/2/009.

[23] S. J. Zinkle, J. Steven, Radiation-Induced Effects on Microstructure, R.J. M. Konings (2012) 65-98.

[24] R. Grieseler, F. Theska, T. Sturzel, B. Hahnlein, M. Hopfeld, T. Kups, J. Pezodt, P. Schaaf, Elastic properties of nanolaminar Cr_2AlC films and beams determined by in-situ scanning electron microscope bending tests, Thin Solid Films 604 (2016) 85–89, https://doi.org/10.1016/j.tsf.2016.03.026.

[25] R. Grieseler, B. Hähnlein, M. Stubenrauch, T. Kups, M. Wilke, M. Hopfeld, J. Pezoldt, P. Schaaf, Nanostructured plasma etched, magnetron sputtered nanolaminar Cr_2AlC MAX phase thin films, Appl. Surf. Sci. 292 (2014) 997–1001, https://doi.org/10.1016/j.apsusc.2013.12.099.

[26] J.F. Ziegler, M.D. Ziegler, J.P. Biersack, SRIM – The stopping and range of ions in matter, Nucl. Instrum. Methods. Phys. Res. B 268 (2010) 1818–1823, https://doi.org/10.1016/j.nimb.2010.02.091.

[27] J. Ehrler, M.O. Liedke, J. Cizek, R. Boucher, M. Butterling, S. Zhou, R. Böttger, E. Hirschmann, T.T. Trinh, A. Wagner, J. Lindner, J. Fassbender, C. Leyens, K. Potzger, R. Bali, The role of open-volume defects in the annihilation of antisites in a B2-ordered alloy, Acta Mater. 176 (2019) 167–176, https://doi.org/10.1016/j.actamat.2019.06.037.

[28] R.W. Siegel, Positron annihilation spectroscopy, Annu. Rev. Mater. Sci. 10 (1980) 393–425, https://doi.org/10.1146/annurev.ms.10.080180.002141.

[29] V.I. Grafutin, E.P. Prokop'ev, Positron annihilation spectroscopy in materials structure studies, Instrum. Methods Invest. 45 (2002) 59, https://doi.org/10.1070/pu2002v045n01abeh000971.

[30] J.V. Olsen, P. Kirkegaard, N.J. Pedersen, M. Eldrup, PALSfit: A new program for the evaluation of positron life-time spectra, Phys. Status Solidi C 4 (2017) 4004–4006, https://doi.org/10.1002/pssc.200675868.

[31] M.O. Liedke, W. Anwand, R. Bali, S. Cornelius, M. Butterling, T. Trinh, A. Wagner, S. Salamon, D. Walecki, A. Smekhova, H. Wende, K. Potzger, Open volume defects and magnetic phase transition in $Fe_{60}Al_{40}$ transition metal aluminide, J. Appl. Phys. 117 (2015) 163908, https://doi.org/10.1063/1.4919014.

[32] A. Wagner, M. Butterling, M.O. Liedke, K. Potzger, R. Krause-Rehberg, Positron annihilation lifetime and Doppler broadening spectroscopy at the ELBE facility, in: International Workshop on Physics with Positrons at Jefferson Lab, 2018. doi: 10.1063/1.5040215.

[33] Q.T.H. Ta, N.M. Tran, J.-S. Noh, Pressureless manufacturing of Cr_2AlC compound and the temperature effect, Mater. Manuf. Process. 36 (2021) 200–208, https://doi.org/10.1080/10426914.2020.1819547.

[34] J. Gonzalez-Julian, S. Onrubia, M. Bram, O. Guillon, Effect of sintering method on the microstructure of pure Cr_2AlC MAX phase ceramics, J. Ceram. Soc. Jpn. 124 (2016) 415–420, https://doi.org/10.2109/jcersj2.15263.

[35] K. Sobolev, A. Pazniak, O. Shylenko, V. Komanicky, A. Provino, P. Manfrinetti, D. Peddis, V. Rodionova, Complex optimization of arc melting synthesis for bulk Cr_2AlC MAX-phase, Ceram. Int. 47 (2021) 7745–7752, https://doi.org/10.1016/j.ceramint.2020.11.119.

[36] T. Cabioch, P. Eklund, V. Maucham, M. Jaouen, M.W. Barsoum, Tailoring of the thermal expansion of $Cr_2(Al_x, G_{e1-}x)C$ phases, J. Eur. Ceram. Soc. 33 (2013) 897–904, https://doi.org/10.1016/j.jeurceramsoc.2012.10.008.

[37] T. Korhonen, M.J. Puska, R.M. Nieminen, First-principles calculation of positron annihilation characteristics at metal vacancies, Phys. Rev. B Condens. Matter 54 (1996) 15016–15024, https://doi.org/10.1103/PhysRevB.54.15016.

[38] M. Bugnet, V. Mauchamp. E. Oliviero, M. Jaouen, T. Cabioc'h, Chemically sensitive amorphization process in the nanolaminated Cr_2AlC (A=Al or Ge) system from TEM in situ irradiation, J. Nucl. Mater. 441 (2013), 133-137. doi: 10.1016/j.jnucmat.2013.05.028.

[39] R. Krause-Rehberg, H.S. Leipner, Positron annihilation in semiconductors: defect studies, 1, Springer, Berlin, Heidelberg, 1999.

[40] T.C. Leung, Z.A. Weinberg, P. Asoka-Kumar, B. Nielsen, G.W. Rubloff, K.G. Lynn, Positron annihilation at the Si/SiO_2 interface, J. Appl. Phys. 71 (1992) 530–532, https://doi.org/10.1063/1.350694.

[41] R. A. Hakvoort, H. Schut, A. van Veen, W. M. Arnold Bik, F. H. P. M. Habraken, Positron annihilation study of low pressure chemical vapor deposited silicon nitride films, Appl. Phys. Lett. 59 (1991), 1687-1689. doi: 10.1063/1.106218.

[42] J. S. Cabaco, *et al*, 2024 (in preparation).

[43] Lee, W.E., Giorgi, E., Harrison, R., Maître, A. and Rapaud, O. (2014). Nuclear Applications for Ultra-High Temperature Ceramics and MAX Phases. In Ultra-High Temperature Ceramics (eds W.G. Fahrenholtz, E.J. Wuchina, W.E. Lee and Y. Zhou). doi: 10.1002/9781118700853.ch15.

[44] D. J. Tallman (2015), On the potential of MAX phases for nuclear applications, Drexel University.

[45] E.N. Hoffman, D.W. Vinson, R.L. Sindelar, D.J. Tallman, G. Kohse, M.W. Barsoum, MAX phase carbides and nitrides: Properties for future nuclear power plant in-core applications and neutron transmutation analysis, Nucl. Eng. Des. 244 (2012) 17–24, https://doi.org/10.1016/j.nucengdes.2011.12.009.

[46] S.J. Zinkle, Advanced irradiation-resistant materials for generation IV nuclear reactors, Struct. Mater. Generation IV Nuclear Reactors (2017) 569, https://doi.org/10.1016/B978-0-08-100906-2.00016-1.

[47] J.G. Gigax, M. Kennas, H. Kim, T. Wang, B.R. Maier, H. Yeom, G.O. Johnson, K. Sridharan, L. Shao, Radiation response of Ti_2AlC MAX phase coated Zircaloy-4 for accident tolerant fuel cladding, J. Nucl. Mater. 523 (2019) 26–32, https://doi.org/10.1016/j.jnucmat.2019.05.021.

[48] Munagala, S.P. (2017). MAX Phases: New Class of Carbides and Nitrides for Aerospace Structural Applications . In: Prasad, N., Wanhill, R. (eds) Aerospace Materials and Material Technologies. Indian Institute of Metals Series. Springer, Singapore. doi: 10.1007/978-981-10-2134-3_20.

[49] W. Hu, Z. Huang, Y. Wang, X. Li, H. Zhai, Y. Zhou, L. Chen, Layered ternary MAX phases and their MX particulate derivative reinforced metal matrix composite: A review, J. Alloy. Compd. 856 (2021) 157313, https://doi.org/10.1016/j.jallcom.2020.157313.

[50] M. Roknuzzaman, M. A. Hadi, M. J. Adben, M. T. Nasir, A. K. M. A. Islam, M. S. Ali, K. Ostrikov, S. H. Naqib, Physical properties of predicted Ti_2CdN versus existing Ti_2CdC MAX phase: An *ab initio* study 133 (2016), 148–153. doi: 10.1016/j.commatsci.2015.11.039.